REPORT DOCUMENTATION PAGE

Form Approved
OMB No. 0704-0188

1. AGENCY USE ONLY *(LEAVE BLANK)*	2. REPORT DATE	3. REPORT TYPE AND DATES COVERED
	9 May 1995	Professional Paper

4. TITLE AND SUBTITLE

Anemometer Design Using the Aerodynamic Drag of Circular Cylinders with Vortex Controlling Surface Protrusions

5. FUNDING NUMBERS

6. AUTHOR(S)

Robert E. Lake

7. PERFORMING ORGANIZATION NAME(S) AND ADDRESS(ES)

DEPARTMENT OF THE NAVY
NAVAL AIR WARFARE CENTER AIRCRAFT DIVISION
PATUXENT RIVER, MARYLAND 20670-5304

8. PERFORMING ORGANIZATION REPORT NUMBER

9. SPONSORING/MONITORING AGENCY NAME(S) AND ADDRESS(ES)

10. SPONSORING/MONITORING AGENCY REPORT NUMBER

11. SUPPLEMENTARY NOTES

12a. DISTRIBUTION/AVAILABILITY STATEMENT

APPROVED FOR PUBLIC RELEASE; DISTRIBUTION IS UNLIMITED.

12b. DISTRIBUTION CODE

13. ABSTRACT *(Maximum 200 words)*

A series of wind tunnel and flight tests were conducted to determine the ability of four anemometer configurations to accurately measure helicopter rotor downwash outflow magnitude and direction. The anemometers were designed to use the aerodynamic drag produced on a circular cylinder as the sensing stimulus. The non-linearities in drag with respect to Reynolds numbers that are associated with smooth cylinder flow were overcome by incorporating vortex controlling surface protrusions. The four surface protrusion configurations discussed here include vertical flutes, helical strakes, and small and large grid mesh. Measurement performance was quantified by determining the sensor's range, calibration accuracy, linearity, frequency response, accuracy in measuring angle of wind incidence, and ability to correct angle of attack induced errors. Testing demonstrated that the four configurations show comparable downwash measuring performance to the ion beam deflection anemometer. Although the sensor's design was intended for measuring helicopter rotor downwash, the results from this paper can be applied to a variety of high velocity measurement applications as well.

14. SUBJECT TERMS

Anemometer, downwash, drag sensor

15. NUMBER OF PAGES

21

16. PRICE CODE

17. SECURITY CLASSIFICATION OF REPORT	18. SECURITY CLASSIFICATION OF THIS PAGE	19. SECURITY CLASSIFICATION OF ABSTRACT	20. LIMITATION OF ABSTRACT
UNCLASSIFIED	UNCLASSIFIED	UNCLASSIFIED	UL

ANEMOMETER DESIGN USING THE AERODYNAMIC DRAG OF CIRCULAR CYLINDERS WITH VORTEX CONTROLLING SURFACE PROTRUSIONS

R.E. LAKE

Naval Air Warfare Center, Patuxent River, Maryland

Summary

A series of wind tunnel and flight tests were conducted to determine the ability of four anemometer configurations to accurately measure helicopter rotor downwash outflow magnitude and direction. The anemometers were designed to use the aerodynamic drag produced on a circular cylinder as the sensing stimulus. The non-linearities in drag with respect to Reynolds numbers that are associated with smooth cylinder flow were overcome by incorporating vortex controlling surface protrusions. The four surface protrusion configurations discussed here include vertical flutes, helical strakes, and small and large grid mesh. Measurement performance was quantified by determining the sensor's range, calibration accuracy, linearity, frequency response, accuracy in measuring angle of wind incidence, and ability to correct angle of attack induced errors. Testing demonstrated that the four configurations show comparable downwash measuring performance to the ion beam deflection anemometer. Although the sensor's design was intended for measuring helicopter rotor downwash, the results from this paper can be applied to a variety of high velocity measurement applications as well.

1. INTRODUCTION

The measurement of external flow can be accomplished using any of an assortment of sensors (anemometers). Most are designed for specialized measurement applications such as aircraft airspeed (pitot-static tube), atmospheric winds (rotating cup, hot film, and ion beam deflection anemometers), and fluid dynamic studies (hot-wire anemometer and laser velocimeters). This paper will discuss the development of sensors designed for measuring the outflow characteristics of helicopter rotor downwash flow fields. The results may be relevant to additional measuring applications such as high velocity ambient wind (tornado and hurricane) as well.

Downwash anemometers must be rugged enough to withstand large magnitude winds (greater than 120 knots) and be able to withstand helicopter generated flying debris. Additionally, the sensor must be able to accurately measure wind in a 360 degree plane and be correctable if the wind is incident at an angle of attack greater than zero. Downwash winds pulsate[1] so the sensor must have a relatively fast response time (10 hz or greater). Past testing on rotating cup[2] and hot-film anemometers show they give adequate angular measurement performance but lack the response time to accurately capture flow field dynamics. The ion beam deflection anemometers behave exceptionally well within all the above constraints and have proved extremely successful with past helicopter downwash tests.

For current helicopter test programs it has become necessary to design a new anemometer system because the ion beam sensor is no longer commercially available. The new anemometer design is based on the theory that a circular cylinder engulfed in a flow field is effected by a dynamic pressure which can be translated into a measurable drag force. The major problem encountered with flow measurement on the circular cylinder is the drag force is non-linear with respect to velocity squared due to lee side vortex formation. This deviation from linearity may lead to a requirement for high order calibration curves which are normally undesirable in instrumentation applications.

This paper will describe the design criteria and performance of four dynamic pressure sensor configurations with major emphasis on vortex control techniques to obtain relatively constant drag coefficients.

2. VORTEX FORMATION

Figure 1 shows a plot of C_D versus the Reynolds number (Re_D) for a smooth circular cylinder. The corresponding flow phenomena is shown in figure 2.

Type A flow (Reynolds numbers below 1) is evidenced by laminar flow both upstream and downstream This flow closes in smoothly behind the cylinder. Large viscous forces as compared to inertial forces are present due to the viscous shear stress at the wall.

Type B flow (Reynolds numbers between 3 and 40) shows the drag coefficient decreasing as the inertial forces become stronger. A pair of steady, attached vortices appear in the wake.

Type C flow (Reynolds numbers between 30 and 90) shows an ultimate slow viscous decay as the drag coefficient is decreased further. The twin attached vortices start to vibrate irregularly and become unstable.

Type D flow (Reynolds numbers between 80 and 300) occurs when the vortices break off periodically, alternating from either side. The laminar boundary layer separates behind the cylinder.

Type E flow (Reynolds numbers between 150 and 130,000) starts the process of transition to turbulent flow. Two shear layers are formed from the energetic outer stream to the slow moving wake. These layers produce lines of vortices which become unstable and disorderly, forming a free turbulent* wake. The separation point is approximately 90 degrees from the leading stagnation point. The maximum low pressure region occurs behind the cylinder.

Type F flow (Reynolds numbers between 100,000 and 3,500,000) shows a dramatic drop in C_D. A separation bubble is formed after the boundary layer reattaches itself after initial separation enclosing a small recirculating flow[3]. The bubble produces a narrowing of the wake which decreases the pressure differential across the cylinder. The decrease in pressure leads to the sharp fall in drag coefficient.

Type G flow (Reynolds numbers greater than 3,500,000) eliminates the separation bubble and the turbulent part of the boundary layer slowly moves forward, thus regenerating the larger pressure differential and increasing C_D.

---

* free turbulence refers to turbulence from the interaction of fluids and not that portion of the boundary layer which is turbulent.

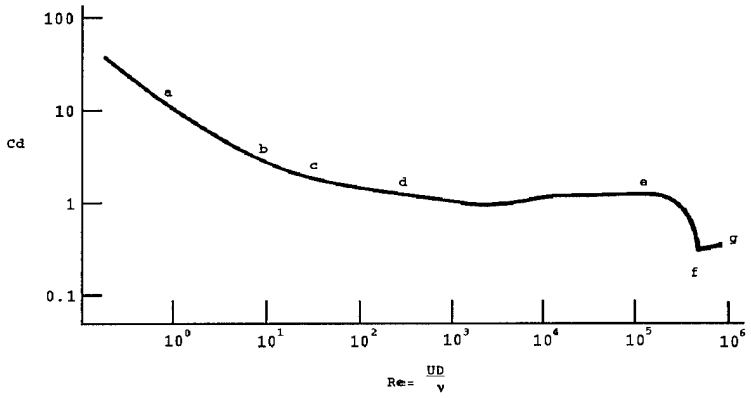

Figure 1
Drag Coefficient for 2-Dimensional Flow Around a Smooth Circular Cylinder[4]

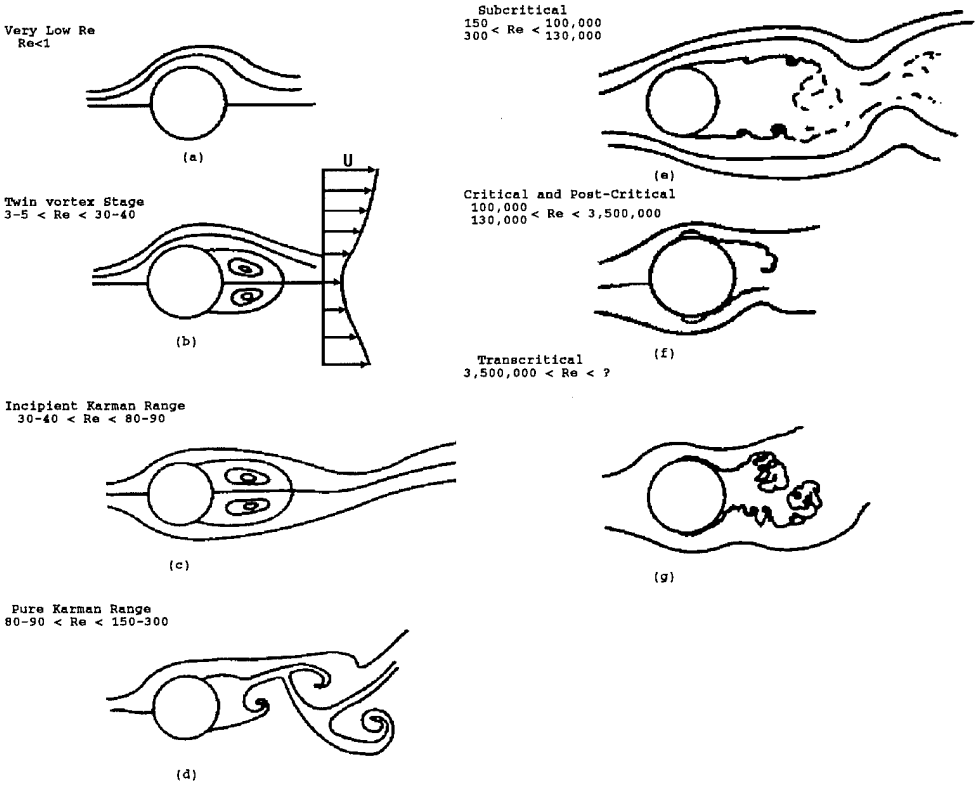

Figure 2
Summary of Major Reynolds Number Regimes[5]

For downwash applications, the sensor will operate in the subcritical to transcritical flow regimes. The basis of sensor head design was to control vortex formation by interrupting the recirculating flow that produces the separation bubble. This will allow the flow to operate in the fully turbulent, transcritical flow regime.

To effectively control vortex formation, energy must be supplied to the laminar boundary layer to form a turbulent boundary layer. Energy can be supplied to the laminar layer by vibrating the body, vacuum off the boundary layer, engulfing the body in unsteady flow, or as chosen for these designs, produce an unsteady flow forward of the body by surface protrusions (trip the boundary layer). Three types of surface protrusions are studied in this paper: flutes, helical strakes, and a mesh shroud. The latter two have circumferential grooving to allow retention of some two dimensional flow characteristics at angles of attack that are greater or less than zero degrees.

3. SENSORS

3.1 Drag Sensor

The design premise was to produce an aerodynamic drag force on a circular cylinder such that a corresponding electrical output could be measured from four column mounted strain gages. The strain gage arrangement allowed determination of flow magnitude and direction through resolution of the x (0 degrees) and y (90 degrees) output voltage components.

Figure 3.1 shows the three sensors which incorporate vortex controlling surfaces. The fluted cylinder shown in figure 3(a) was the first design iteration. Subsequent investigation of vortex controlling techniques lead to the design of the helical strake and the mesh shroud cylinder heads, shown in figure 3(b) and 3(c) respectively.

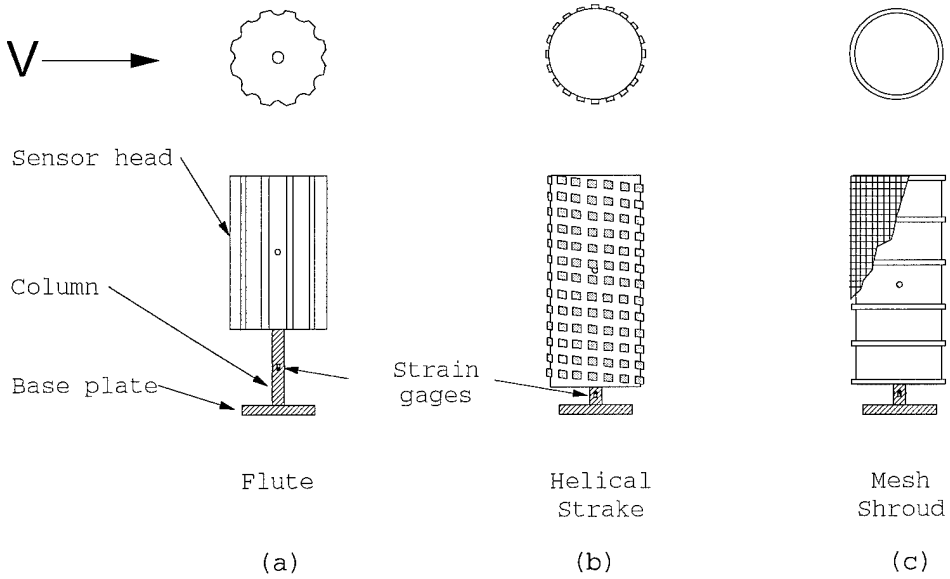

Figure 3.
Sensor Configurations

All of the cylindrical heads were approximately four inches in diameter and manufactured from Type-101 nylon stock. To develop a larger drag force, the flute head length was increased from six inches to nine inches for the helical strake and mesh shroud heads. The flute head had 3/8 inch radii vertical grooves at 30 degree increments. Likewise, every 30 degrees the helical strake had 1/4x1/4 inch vertical grooves cut into the 1/4x1/4 inch by 1.75 thread per inch helix. The two configurations of the mesh shroud heads were fitted with a 1/16 inch diameter stainless steel wire mesh with small and large meshes of 1/8x1/8 inch and 1/4x1/4 inch grids, respectively.

The flute sensor's strain gages were mounted on the 0.5 inch diameter aluminum column at a position 1.5 inches above the base plate. The helical strake and mesh shroud sensors' strain gages were lowered to 0.75 inches above the base plate to improve low speed measurements.

The heads were affixed to the column by a 1/16 inch diameter aluminum roll pin that was located six inches above the base plate. The three inch diameter by 3/8 inch thick aluminum base plate was welded to the column. The base plate incorporated four 11/32 inch diameter holes that mated to either the wind tunnel test apparatus or downwash cart sensor mounts.

During initial wind tunnel tests the flute anemometer showed a high susceptibility to vibrational noise. The forcing function was primarily caused by wind tunnel vibration as the tunnel's test section was not equipped with any substantial damping apparatus. The frequency spectra revealed the sensor's natural frequency existed at approximately 26 hz. The mass was subsequently reduced to increase the natural frequency to approximately 32 hz. Mass reduction was performed by boring vertical holes in the sensor head. The holes were capped off to prevent unwanted pressure fluctuations.

Once the natural frequency was localized, a signal conditioner was fabricated to: provide the 10 VDC bridge excitation, provide a 660 strain gage amplification, and pass the signal through a 10 hz, 6-pole Butterworth filter. Figure 4 shows the frequency response of the filter.

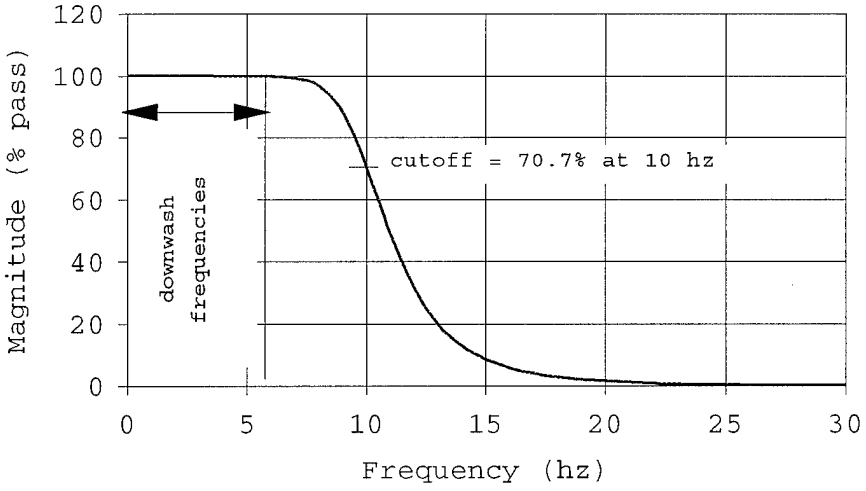

Figure 4
Butterworth Filter Frequency Response

3.2 Ion Beam Deflection Anemometer

The ion beam deflection anemometer was considered by Naval Air Warfare Center Patuxent River, to be one of the best two axis instruments for measuring rotor downwash velocity and direction. To determine the drag sensor's potential for becoming a replacement downwash sensor, drag sensor test data was evaluated against ion beam sensor performance.

The ion beam anemometer functioned on the principle of projecting a beam of ionized molecules across an air gap in a direction perpendicular to the airflow. The ionized molecules were collected onto a resistive two-dimensional grid after transiting the air gap and after being carried downstream from their point of injection. A current was generated in the grid and amplified to produce an *x* and *y* voltage output proportional to wind speed. The ion beam had a 35 hz frequency response.

4.0 EXPERIMENTAL PROCEDURES

4.1 Wind Tunnel Tests

Wind tunnel tests were performed in an open circuit system driven by a 60 inch diameter centrifugal fan powered by a 1200 rpm, 300 horsepower electric motor. The 36 inch test section had a 20 knot minimum and 190 knot maximum air speed. Four wind tunnel tests were performed on each sensor to determine: air speed calibration, proportional limit, angular resolution response, and angle of attack response.

Air speed calibration tests determined the calibration curves and drag coefficients. Each sensor was subjected to incremental airspeeds to obtain the calibration curves that described the output (volts) versus velocity relationship. The sensors were bolted to the angular resolution fixture (figure 5(a)), set at 0 degrees, to acquire the +*x*-axis calibration curve. Data was collected by varying tunnel speeds from 20 to 150 knots in 10 knot increments. The above procedures were repeated to acquire the -*x*-axis, +*y*-axis, and -*y*-axis calibration curves.

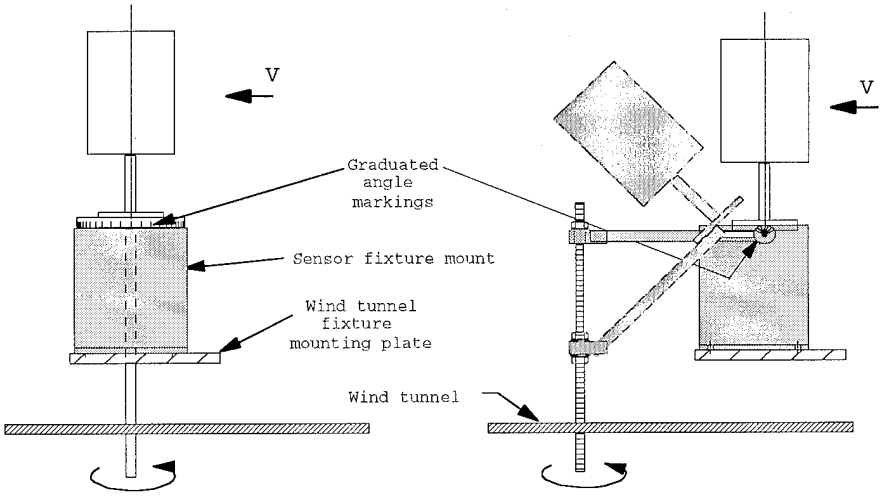

Angular Resolution (a)

Angle of Attack (b)

Figure 5
Wind Tunnel Test Fixtures

Proportional limit tests determined the maximum obtainable airspeed the sensor can be subjected before the column's proportional limit was reached (where local stress is no longer proportional to strain). Each sensor was subjected to incremental mass loading to provide an output versus force relationship. The sensors were horizontally clamped to a rigid surface with the x-axis vertical. Data was collected while incrementing one pound weights until 100 lbs was reached. This experiment was repeated with the *y*-axis vertical. As the weights were slowly applied, the stress-strain curve was plotted and observed for a deviation from linearity, thus indicating the proportional limit.

Angular resolution tests determined the sensor's accuracy while wind is incident at various angles in the horizontal plane. The sensors were mounted to the angular resolution fixture, initially set at 0 degrees relative to wind direction. The wind tunnel was brought up to 20 knots, stabilized, and data was collected while rotating the sensors in 10 degree increments in the horizontal plane through 360 degrees. This experiment was repeated at wind tunnel settings of 60 and 100 knots.

Angle of attack tests determined the sensor's accuracy while wind direction is varying in the vertical plane. The sensors were mounted to the angle of attack fixture (figure 5(b)) with the x-axis parallel to tunnel flow and at a position -40 degrees from vertical. Data was collected while rotating the sensors in 5 degree increments in the vertical plane through +45 degrees. This experiment was repeated at wind tunnel speeds of 20, 60 and 100 knots.

All wind tunnel data were sampled for 2 second at 100 hz and averaged. Calibration, proportional limit, and angle of attack curves were generated by least squared procedures. The sensor's imprecision from the calibration process was defined as the error limit and was specified as three times the standard deviation (σ)of the difference between the actual and indicated velocities. The error limit made the statistical statement that 99.7% of the normally distributed data will lie between 3σ. The angular resolution error limit for both the velocity and angular error was defined as of the differences between indicated and true values (velocity or direction). The angle of attack error limit was defined as 3σ of the difference between the indicated velocity and the correction equation generated velocity. Independent linearity was defined as being the maximum deviation of any data point from the calibration curve, expressed as a percentage of full-scale reading[6].

4.2 Flight Tests

Flight tests were conducted to determine the ability of the drag sensors to accurately measure helicopter rotor downwash flow. Flight tests used a CH-53E Super Stallion as a sensing stimulus, as shown in figure 6.

The instrumentation cart shown in figures 6 and 7 was used to gather helicopter downwash data at various radial distances from the hover site center. The four wheeled instrumentation cart was 10 foot long by 8 foot wide and ballasted to provide stability in high velocity winds. The cart contained a 120 VAC power generator and all applicable signal conditioning equipment. A 7 ft. anemometer mounting pole was placed on the cart at the forward most position to avoid cart generated wind interference. Two paired sets of ion

beam and drag anemometers were mounted on the pole at positions of 3 and 4 feet above ground level (AGL).

The instrumentation cart was positioned as to have the anemometer pole centered on the hover site center. All hover headings were at 270 degrees relative to the cart's longitudinal centerline. To determine the ability of the drag sensor to accurately measure light winds, the aircraft hovered 100 feet AGL and 171 feet from the anemometer pole. Hover was stabilized for one minute to facilitate data collection. The above steps were repeated for the heavy wind condition event where the aircraft was positioned 20 feet AGL and 67 feet from the pole.

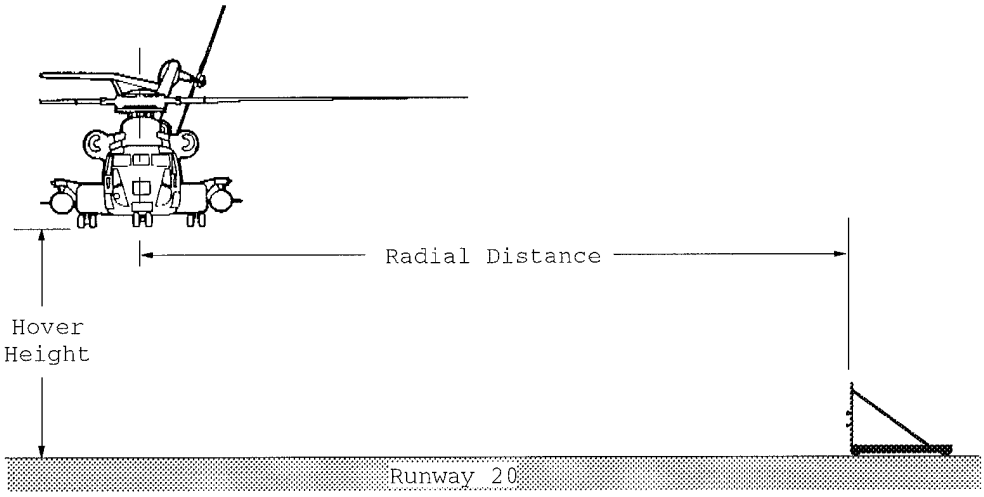

Figure 6
Flight Test Arrangement

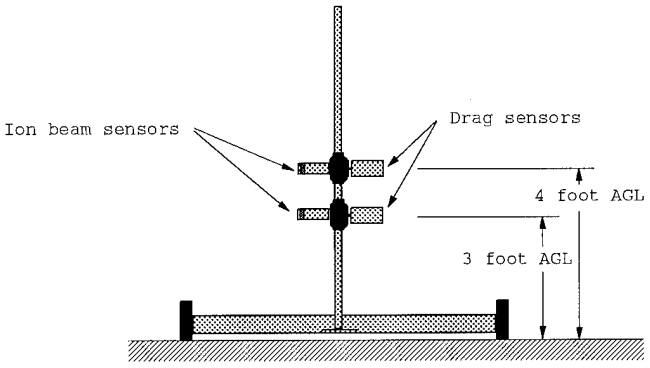

Figure 7
Downwash Cart Sensor Arrangement

5 RESULTS

5.1 Air Speed Calibration

The ability to design a cylinder that has a drag coefficient that does not significantly influence the instrument's calibration is dependent on the vortex control effectiveness. Although vortex "prevention" would be the ultimate design goal, the vortex mechanism seems indestructible: it can be delayed but never destroyed[7].

The designed measuring range of velocities was 20 to 150 knots which relates to Reynolds numbers of $6x10^4$ to $5x10^5$. This region corresponds to the smooth cylinder's subcritical and critical flow regimes. Figure 8 shows the drag sensors' C_D remains non-linear as vortex influence is moving the separation points leeward with increasing Reynolds number. Figure 8 notes that as the smooth cylinder's C_D continues to fall after Re=2.0x10, the drag sensors' C_D begins to approach constant. This occurrence is present because the surface protrusions have inhibited the recirculation process that forms the separation bubble. The drag cylinder's flow proceeds past the critical flow and remains operable in the transcritical regime.

A design consideration was to change the cylinder's diameter to operate solely in either the pure Karman range or the transcritical range. This consideration was rejected due to the Pure Karman range would require a 1 inch diameter cylinder that would not produce enough drag for output clarity and a 57 inch transcritical diameter would be unreasonably large to accommodate on the downwash instrumentation cart.

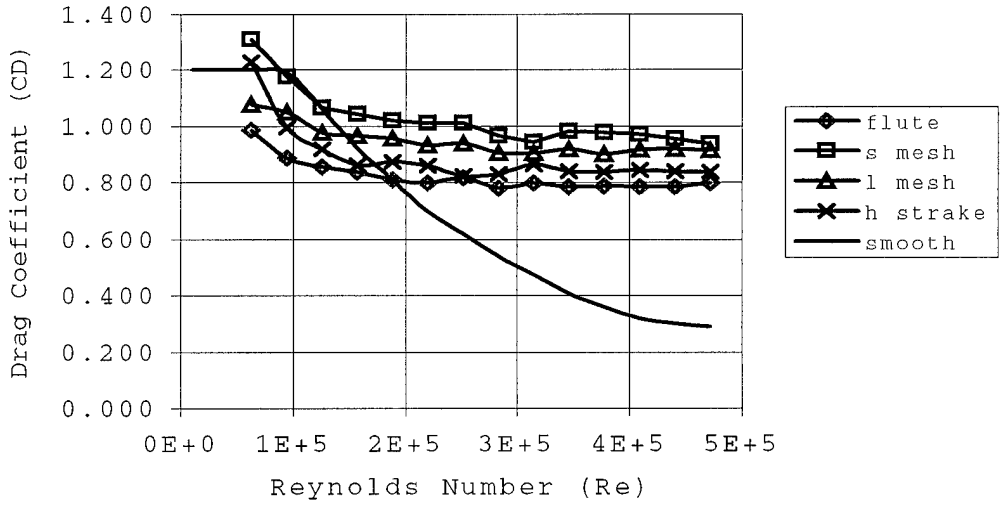

Figure 8
Drag Coefficients

Although the presence and effects of vortex shedding could not be eliminated, minimization of the C_D variance tends to reduce the overall deviation from the calibration curve, as shown in figure 9.

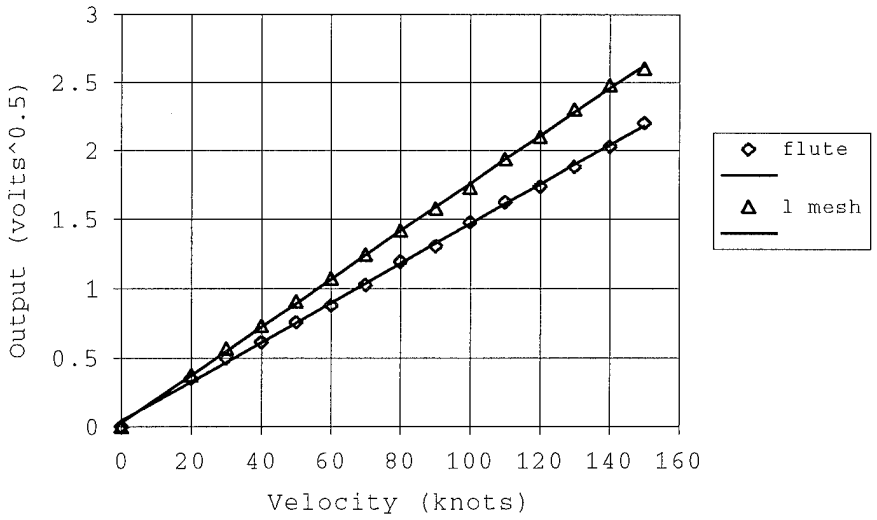

Figure 9
Calibration Curve

For clarity, the small mesh and helical strake configurations were omitted from figure 9 as the outputs are very similar to the large mesh. Two error classifications specify the data point deviation from the calibration curve, the calibration error and the independent non-linearity. The calibration error (figure 10) describes the sensor's accuracy whereas the independent non-linearity (figure 11) describes the deviation from a desired straight line calibration curve. Both deviation specifications characterized measurement error but the independent non-linearity determined if the non-linearities of the C_D versus Re curves had a significant impact on the calibration accuracy.

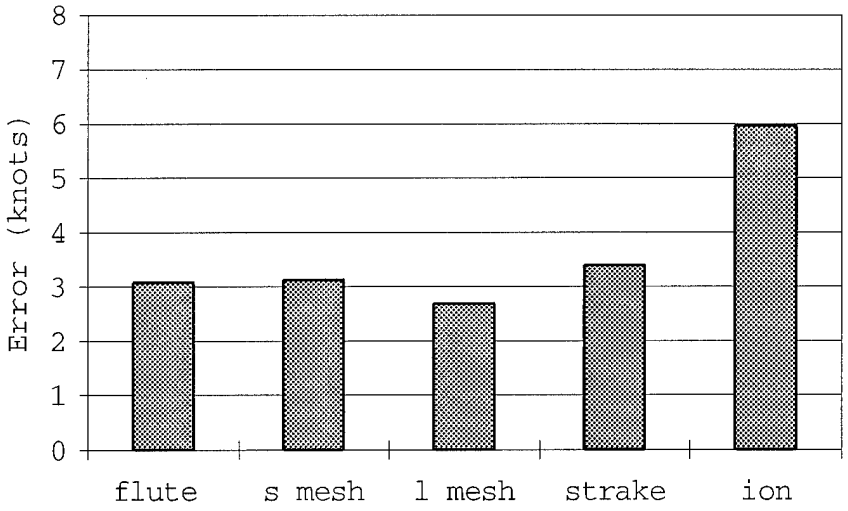

Figure 10
Calibration Error

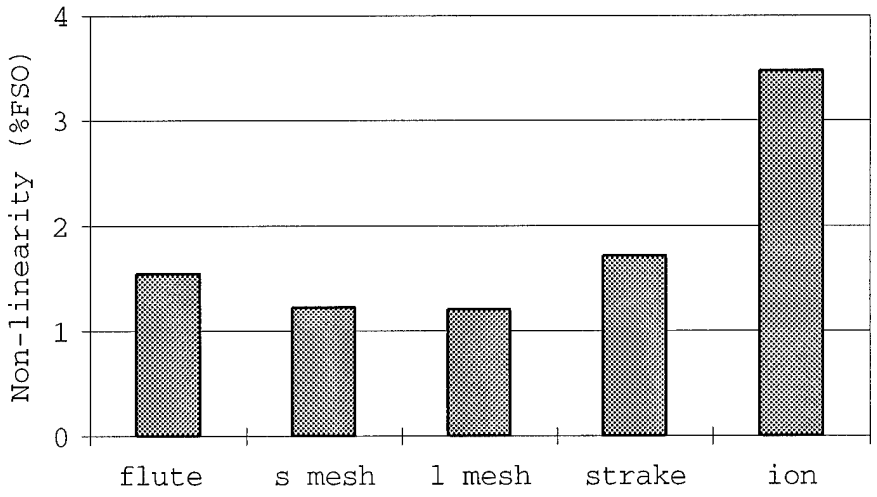

Figure 11
Independent Non-Linearity

Figures 10 and 11 shows the drag sensors have smaller calibration errors and greater tendencies to linear behavior as compared to the ion beam sensor. It should be noted that these particular ion beam sensors have been used for more than 10 years and the effects of age and performance are yet undetermined.

5.2 Proportional Limit

The prototype flute sensor was incrementally loaded from 0 to 100 pounds. The sensor column load did not exceed the proportional limit (detected by a divergence from a straight line) although loading exceeded the theoretical proportional limit (88 pounds) by 12 pounds, as shown in figure 12.

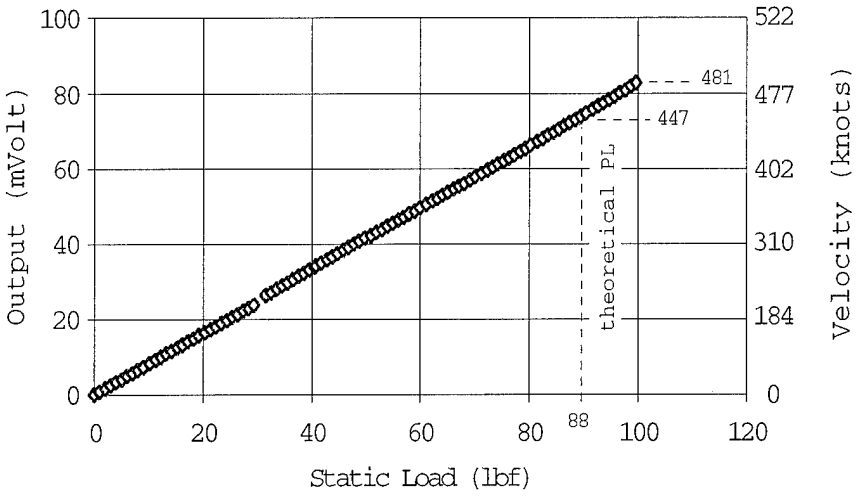

Figure 12
Proportional Limit

The estimated 481 knot maximum velocity is statically determined and does not account for the cyclic fatigue that would be present during pulsating flow. Additionally, the mesh and strake sensors will have a somewhat higher estimated maximum velocity due to the smaller moment created by the lowered center of pressure.

5.3 Angular Resolution

Lift is produced when the lee side pressure distribution shifts slightly to either side of the cylinder. Shifting of the lee side pressure distribution occurs when different surface protrusion patterns appear on the left and right side of the stagnation point. In this instance, boundary layer separation may occur at two distinct angles. This occurrence translates into an error when the strain gage output indicates the velocity direction is slightly offset from the true direction. This lift force is a function of the cylinder's shape as shown in figure 13.

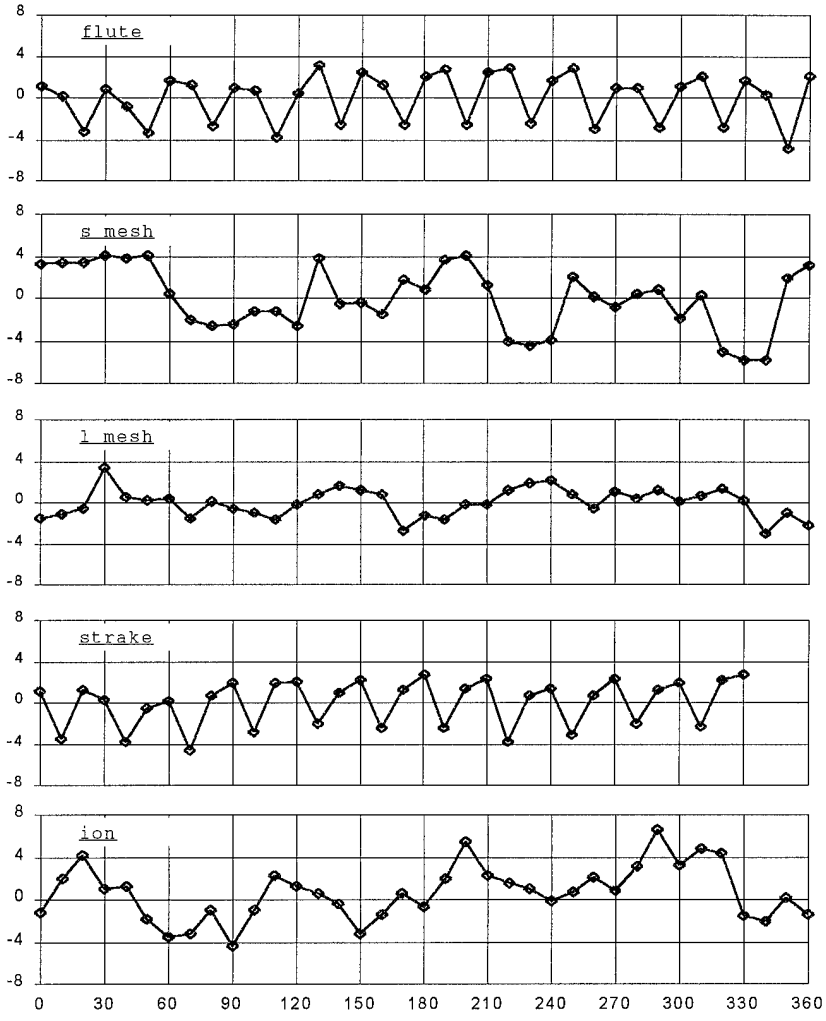

Figure 13
100 Knot Angular Resolution

Figure 13 shows data collected at a 100 knot wind speed. The basic curve shapes remain relatively constant at the remaining test air speeds. Figure 13 also shows the flute and helical strake cylinders have oscillating lift components that correspond to their 30 degree grooving. These geometrically produced errors are not so evident on the mesh sensors but the orientation of the mesh screen generates similar effects with consistency.

The angular resolution error consists of both directional and velocity error components, as shown in figure 14 and 15 respectively.

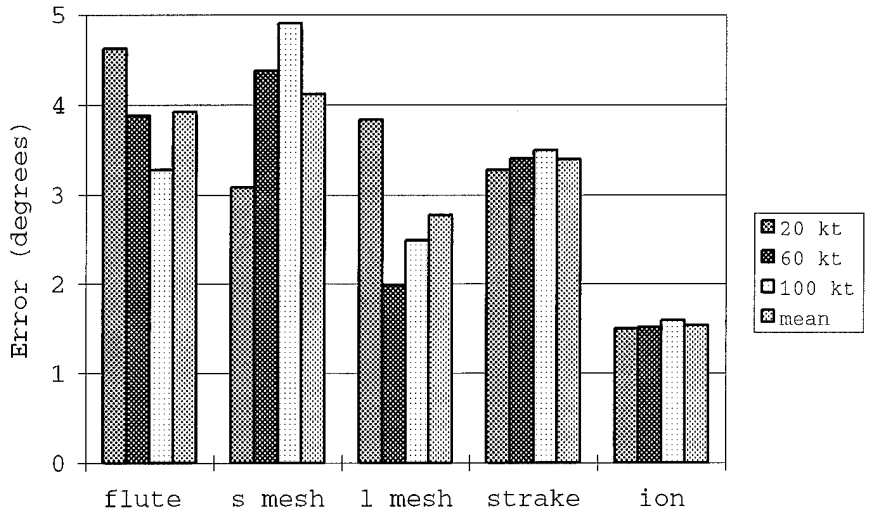

Figure 14
Angular Error

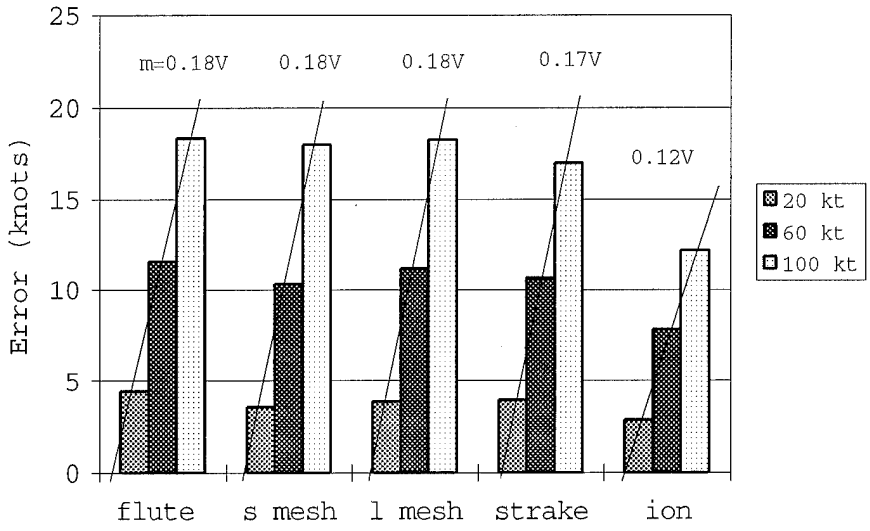

Figure 15
Velocity Error

The angular error appears to be independent of air speed as no definite trends appear. The mean of the three test speed's error determined the average angular error. The angle of incidence velocity error is air speed dependent and is determined by the slope of the velocity versus error curve.

5.4 Angle of Attack

Helicopter rotor downwash flow rarely flows precisely in a radial direction from the helicopter, but has some angular deviation from radial.

These angles may reach ±60 degrees but the wind tunnel test fixture's physical and aerodynamic limitations allowed measurement of only 0 to 45 degrees. The ability of an anemometer to minimize the error associated with wind incident at a specific angle of attack is highly desirable. Figure 16 shows the large mesh sensor normalized output as a function of both angle of attack and wind speed.

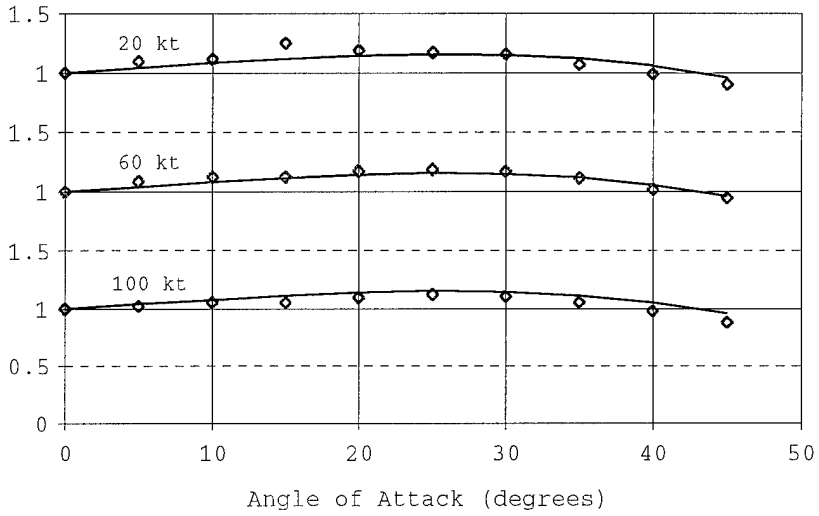

Figure 16
Normalized Angle of Attack Output
(Large Mesh Sensor)

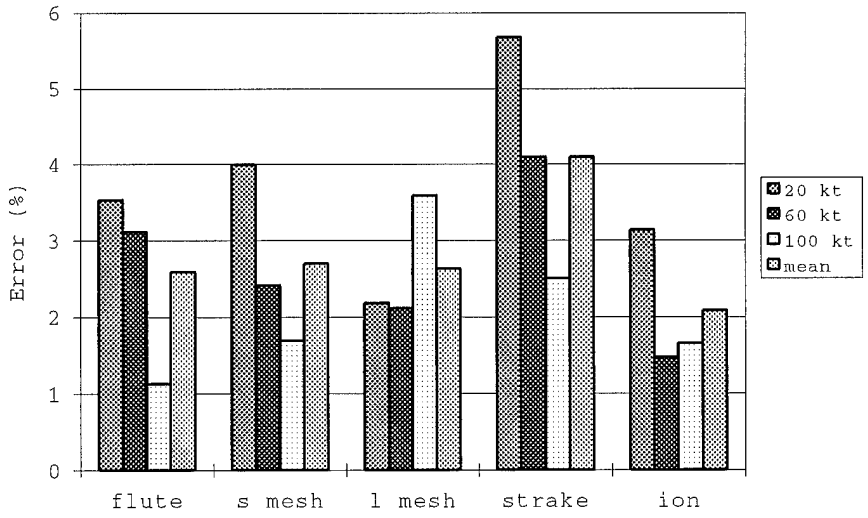

Figure 17
Angle of Attack Error

Although figure 16 represents the large mesh sensor, the results are typical for the other drag sensors. The diamond markers of figure 16 represent test data points and the solid lines represent the output ratio correction equation:

$$q_\phi = \frac{q_i}{\left(a + b\phi + c\phi^2 + d\phi^3\right)}$$

where, $q_\phi \equiv$ AOA corrected output (volts)

$q_i \equiv$ indicated output (volts)

$\phi \equiv$ angle of attack (degrees)

$a, b, c, d \equiv$ curve fit output ratio coefficients

Curvature of the correction equation results from the increased surface area presented due to increased angle of attack. Figure 17 shows the error associated with the data point deviation from the correction equation. The angle of attack error appears to be airspeed independent. The mean of the three test speed's error determined the average angle of attack error.

5.5 Flight Tests

Flight tests were performed with ambient winds out of the northwest at 12 knots with 18 knot gusts and a 78° ambient temperature with a 1625 ft density-altitude. Drag sensor output was corrected for ambient density conditions. Figure 18 shows the velocity magnitude time history and figure 19 shows the velocity direction time history for the heavy wind test event. Low wind test results were very similar but with decreased velocity magnitude.

The velocity magnitude and direction time histories, figures 18 and 19, shows the drag sensor closely tracked the ion beam output. The difference between the two signals was not considered error as the sensors probably experienced slightly different flow fields. The figure also shows a noticeable lag between the sensor outputs. This lag is produced by the phase delay of the electronic filter.

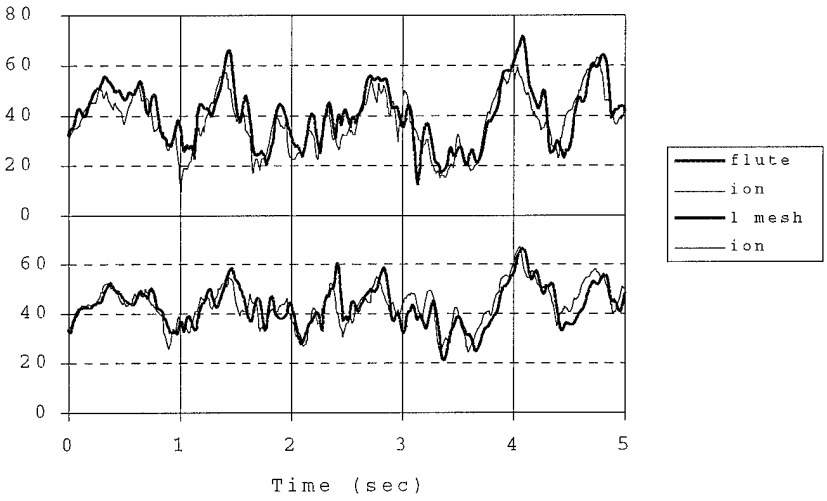

Figure 18
Velocity Magnitude Time History - Heavy Wind
(20 feet AGL Hover, 67 feet Radial Distance)

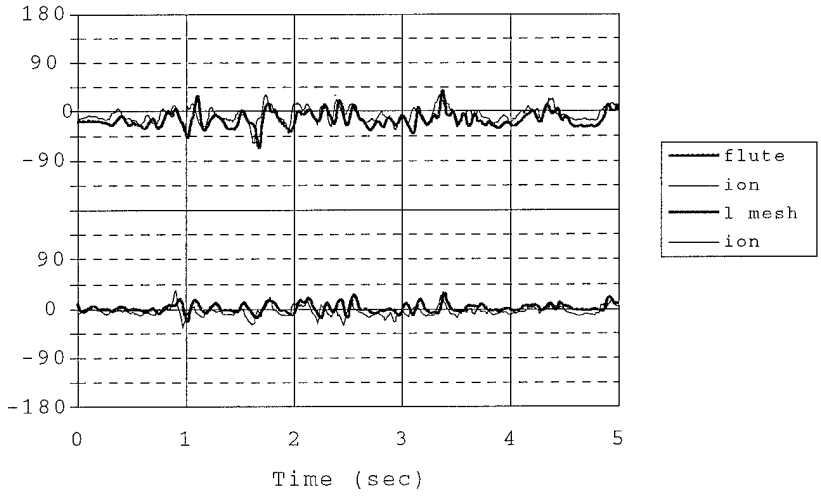

Figure 19
Velocity Direction Time History - Heavy Wind
(20 feet AGL Hover, 67 feet Radial Distance)

Typical rotor downwash flow fields are described with mean and peak flow magnitudes occurring at a specific mean direction. Figure 20 shows a general comparison for the drag and ion beam sensors mean and peak flow measurements. Figure 21 presents a general comparison of mean direction.

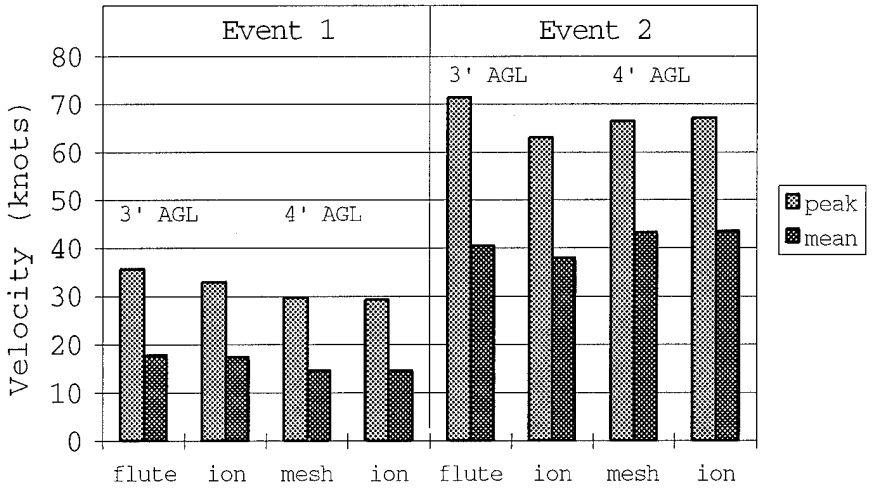

Figure 20
Downwash Mean and Peak Flow Measurement

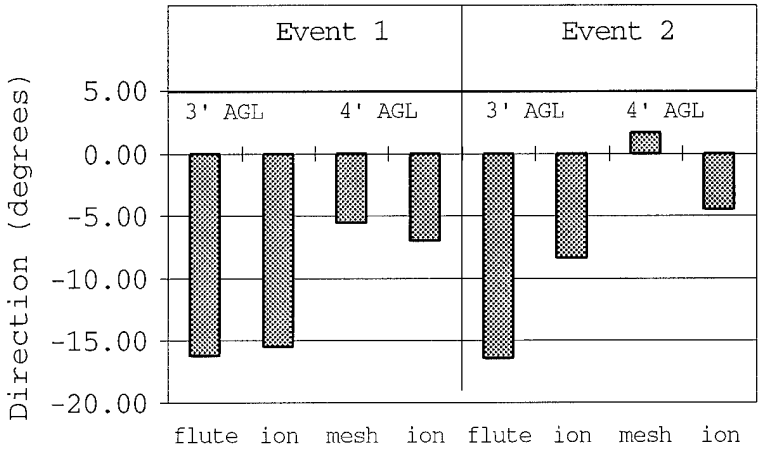

Figure 21
Downwash Direction Measurement

The primary influence of the instability of people engulfed in the downwash flow field is the perturbations (gusts) coupled with large magnitude velocities. The ability of a sensor to accurately capture the flow field dynamics is essential for downwash measurements. Figure 22 shows the large mesh sensor's power spectral density for the heavy wind test event. Although figure 22 describes heavy wind mesh sensor data, results are typical for the flute and mesh sensors for both the low and heavy wind test events.

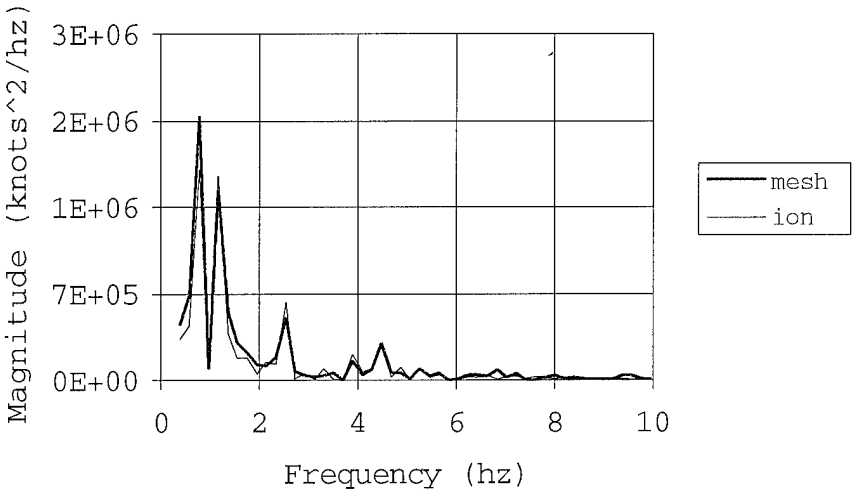

Figure 22
Mesh Sensor Power Spectrum Density - Light Wind
(20 ft AGL Hover, 67 feet Radial Distance)

Figure 22 describes a general comparison of frequency content between the ion beam and drag sensor. The differences between the two data sets are not assumed to be error as differing flow fields and responses characteristics may contribute to slight differences between the power spectral densities. The important aspect of the power spectrum density was to show the drag sensor was capable of measuring the majority of the frequency components contained in a pulsating rotor downwash flow field, typically ranging from 0.1 to 6 hz.

6 CONCLUSIONS

The tests conducted on the four drag sensor configurations produced the technical specifications listed in table 1.

Table 1
Drag Sensor Technical Specifications

	Flute	Small Mesh	Large Mesh	Strake
Range (kt)	20-150	20-150	20-150	20-150
Accuracy (kt)	±(3.1+0.18V)	±(3.1+0.18V)	±(2.7+0.18V)	±(3.4+0.17V)
Non-Linearity (%[1])	1.5	1.2	1.2	1.7
AOI Error (deg)	±3.9	±4.1	±2.7	±3.4
AOA Error (%[2])	2.6	2.8	2.7	4.1
Freq. Resp. (hz)	10	10	10	10

1. Percent full scale output.
2. Percent actual reading.

The *range* values in table 1 were constrained to "as tested" wind tunnel velocities although limited flight testing showed the drag sensors were accurate to as low as 5 knots. Additionally, proportional limit tests indicated the sensor will measure winds in excess of 440 knots.

The vortex control techniques presented in this paper have lead to a higher measuring accuracy as compared to a smooth cylinder design. Different control techniques proved more successful than others in the areas of linear desirability, angular response, and the reduction of calibration error. The large mesh configuration had the best overall performance. Flight testing showed the drag sensor was capable of accurately measuring helicopter downwash mean and peak flow in addition to flow direction. The frequency response of the system (sensor and signal conditioner) was found sufficient for capturing downwash flow perturbations.

The constraints placed on the drag sensor for downwash flow measurement have been met in the areas of: ability to capture high speed wind magnitude and direction, angle of attack correctable, adequate frequency response, and ruggedness. The drag sensor shows excellent performance characteristics as applied to measuring downwash winds and is concluded a low risk, low cost replacement for the ion beam deflection anemometer.

REFERENCES

1. Harris, D.J., Simpson, R.D., "CH-53E Helicopter Downwash Evaluation", NATC-SY-89R-78, Naval Air Test Center, Patuxent River, MD., (1978).

2. Meyerhoff, C.L., Lake, R.E., Gordge, D.N., "Rotorwash Wind Sensor Evaluation", DOT/FAA/RD-93/10, U.S. Department of Transportation, Washington, D.C., (1993).

3. Young, A.D., "Boundary Layers", AIAA Education Series, American Institute of Aeronautics and Astronautics, Washington, D.C. (1989).

4. Binder, R.C., "Fluid Mechanics, Fifth Edition", Prentice-Hall, Englewood, N.J., (1973).

5. Morkovin, M.V., "Flow Around Circular Cylinder - A Kaleidoscope of Challenging Fluid Phenomena", The Martin Company, Baltimore, M.D., (1963).

6. Doebelin, E.O., "Measurement Systems Application and Design", McGraw-Hill, New York, N.Y. (1990).

7. Zdravkovich, M.M., "Review and Classification of Various Aerodynamic and Hydrodynamic Means for Suppressing Vortex Shedding", IAWE, vol.7, (1981), pg.145.